Earthquakes and Structures, *Vol. 9, No. 6 (2015) 1313-1336*
DOI: http://dx.doi.org/10.12989/eas.2015.9.6.1313

Theoretical analysis of self-centering concrete piers with external dissipators

Zhiliang Cao[2a], Tong Guo[*1,2], Zhenkuan Xu[2b] and Shuo Lu[2c]

[1]*Key Laboratory of Concrete and Prestressed Concrete Structures of the Ministry of Education, Southeast University, Nanjing, 210096, P. R. China*
[2]*School of Civil Engineering, Southeast University, Nanjing, 210096, P. R. China*

(Received May 28, 2015, Revised July 27, 2015, Accepted September 4, 2015)

Abstract. The self-centering prestressed concrete (SCPC) bridge pier with external dissipators is a novel structure, aiming at reducing residual deformation and facilitating the post-earthquake repair. This paper presents the configuration and mechanical behaviors of the pier. A theoretical model for the lateral force-displacement relationship under cyclic loading is developed. The proposed model comprises an iterative procedure which describes the deformation of dissipators under different conditions. Equations of pier stiffness after gap opening, as well as the equivalent viscous damping ratio, etc., are derived based on the proposed model. Existing cyclic load test results were used to validate the proposed model, and good agreement is observed between the analytical and test results.

Keywords: theoretical analysis; self-centering; concrete pier; external dissipators

1. Introduction

In recent years, precast bridge pier using unbonded post-tensioned (PT) tendons has been proved to be a promising candidate for modern bridge structures for its remarkable seismic behavior. Instead of forming plastic hinge around the joint zones, large structural deformation demand is accommodated by the column rigid body rotation. Unbonded PT tendons inside the column provide self-centering capacity and pull the pier back to the original position when lateral load is removed. As a result, precast pier is characterized by gap opening and closing at member interface in the event of a ground motion, and negligible residual deformation is observed after earthquake, enabling rapid operation without extensive rehabilitation; while for monolithic piers, undesirable permanent deformation may result in repair problem or even reconstruction (Kawashima *et al*. 1998). Besides, potential advantages of precast pier include shortened construction schedule, improved component quality and reduced environmental pollution, making it a suitable choice especially in highly congested urban regions. These advantages have been

∗Corresponding author, Professor, E-mail: guotong@seu.edu.cn
[a]Ph.D. Candidate, E-mail: 230159067@seu.edu.cn
[b]Postgraduate Researcher, E-mail: xuzhenkuan2012@163.com
[c]Postgraduate Researcher, E-mail: 860978413@qq.com

http://www.techno-press.org/journals/eas&subpage=7 ISSN: 2092-7614 (Print), 2092-7622 (Online)

mentioned in investigations on precast building structures (Kurama *et al*. 2006, Palermo *et al*. 2006, Sritharan *et al*. 2007).

So far many experimental studies have validated the superiority of precast pier (Palermo *et al*. 2005, Ou 2007, Ou *et al*. 2009, Marriot *et al*. 2009, Chou and Chen 2006, EIGawady *et al*. 2010), meanwhile a number of analytical models have been proposed to investigate the behavior of this novel system. In the research conducted by Mander and Chen (1997), minimal energy dissipation and a sharp decrease in the lateral stiffness are described through a bilinear force-displacement curve. Priestley and Tao (1993) conducted a section analysis for precast connection with trilinear idealization which is characterized by three points, namely decompression, linear limit and limit of proportionality of PT steel. A similar model including three key states of column response was validated and refined by considering the accidental eccentricity of axial load (Hewes and Priestley 2001). Within the PRESSS (PREcast Seismic Structural System) program, a "hybrid system" was proposed in which additional dissipators were added into the pure unbonded PT structure, resulting in a "flag-shaped" hysteretic hoop (Standon *et al*. 1997). A lumped plasticity model for precast pier was given by Palermo *et al*. (2007), where the column is modeled using an elastic beam with two rotational springs at base in parallel: "recentering" spring assigned with nonlinear elastic rule models the restoring force, while "dissipative" spring is modeled depending on the type of dissipators. An iterative procedure based on member equilibrium and compatibility was proposed by Pampanin *et al*. (2001), and it was adopted by New Zealand concrete standard (NZS 2006). Ozden and Ertas (2010) further improved the procedure by considering residual deformation, where the dissipator was assigned with the modified Takeda rule (Takeda *et al*. 1970). Chou and Hsu (2008) established a hysteretic model considering stiffness degradation.

Among the aforementioned research efforts, external dissipators have received more and more attention since that they can be replaced readily after an earthquake; and therefore, a novel self-centering precast concrete (SCPC) pier with external energy dissipators and enhanced durability is proposed (Guo *et al*. 2015). However, the analytical work on the behavior of external dissipators under cyclic loading is relatively limited. In this paper, the theoretical model of lateral force-displacement relationship of SCPC pier is developed, in which an iterative procedure considering the deformation of dissipators at different condition is adopted. Expressions for lateral stiffness after gap opening and equivalent viscous damping ratio are also derived. The proposed theoretical model is finally validated through existing low cyclic test results.

2. Configuration of proposed SCPC pier

Fig. 1 shows a schematic drawing of the proposed pier. The concrete column with rectangular section could be factory prefabricated, and unbonded PT FRP tendons are used to precompress the column to the foundation at bridge site. The pier behaves like a monolithic one until seismic load exceeds a certain value, and thereafter gap opening occurs at the bottom of pier. To avoid concrete crushing during rocking, pier bottom segment is encased in a fiber reinforced polymer (FRP) jacket. Reinforced concrete (RC) corbels with ED ducts are field cast above the jacket to provide upper anchorage for the dissipators. An aluminum bar is inserted into the corbel duct and fastened by two bolts, and bottom of the bar is connected to the embedded threaded rod through a connecting sleeve. Cross section of the bar is locally reduced to realize controlled plastic deformation, and the weakened length is wrapped by a confining tube to prevent buckling under compression. In this way the dissipating bar could be easily replaced and installed if damaged after

an earthquake. The installation of the ED bar is illustrated in Fig. 1(b).

3. Analytical model

Fig. 2(a) shows the moment-rotation (M-θ) relationship at column bottom under cyclic loading. Hysteretic loop is characterized by the "double-flag" shape, where self-centering capacity is provided by the PT tendons with bilinear hysteretic behavior, while dissipating capacity comes from the aluminum bars with assumed rhombus-shaped hysteretic behavior. Fig. 2(b) presents the lateral force-displacement (F-Δ) relationship at column top, where G represents the weight of superstructure and F represents the inertial force due to horizontal earthquake. Apart from rigid body rotation, Δ comprises bending deformation of the column. Event 1 is defined as "decompression", where stress of the extreme fiber away from the rotation toe is zero. Prior to event 1, the gap at column-foundation interface keeps closed and behavior of SCPC pier is similar to that of a RC pier, which indicates a linear relationship between F and Δ. After decompression, the gap starts to open and lateral displacement consists of rigid body rotation as well as bending deformation of the column. Neutral axis is gradually removed to the rotation toe, and a nonlinear relationship of F-Δ is observed. Deformation capacity of the pier is controlled by the displacement at event 3, which is determined according to the ultimate strain of prestressed tendon or collapse-prevention performance level of the bridge. If unloading occurs at event 2 prior to 3, Δ is gradually reduced by the restoring force, and area surrounded by curve 1-2 and 2-4 is equal to the dissipated energy. At event 4, the gap is closed again. If the ratio between self-centering force and dissipator force is designed properly, residual drift is negligible at event 5 when lateral force is removed. A similar behavior can be derived for reversed loading.

3.1 Decompression

The rocking begins when stress of the outermost fiber away from the rotation toe is zero at event 1. As shown in Fig. 3, linear strain distribution according to the plane section assumption

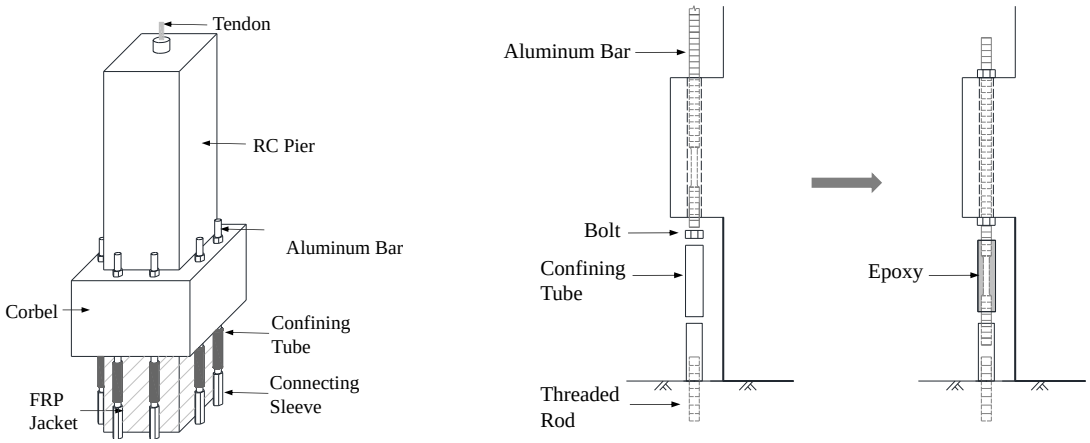

(a) 3D profile (b) Installation of an ED bar

Fig. 1 Schematic drawing of SCPC pier

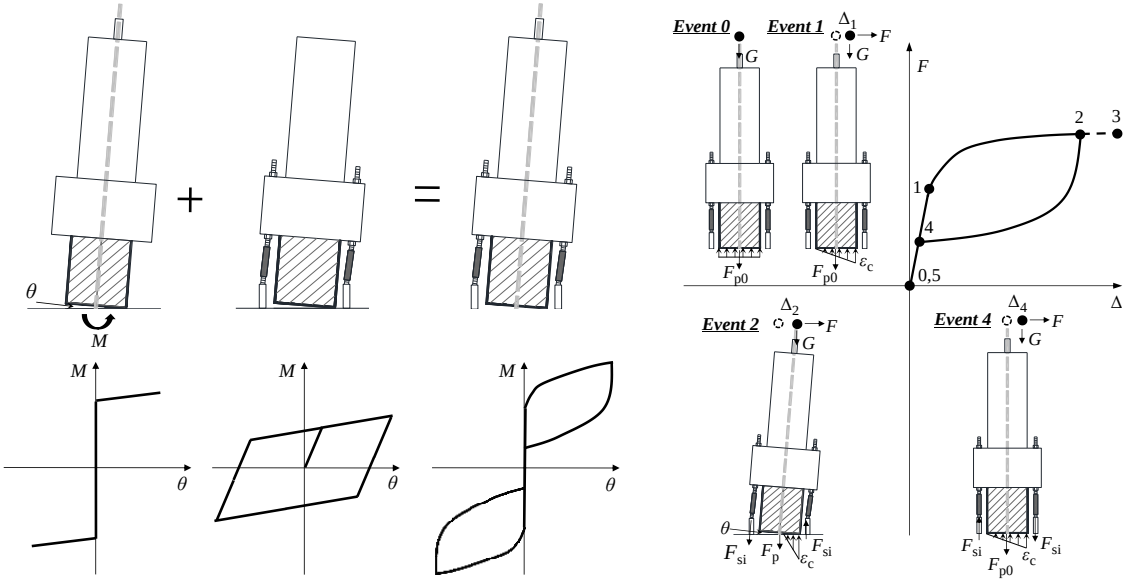

(a) M-θ relationship (b) F-Δ relationship

Fig. 2 Hysteric behaviour of SCPC pier in one cycle

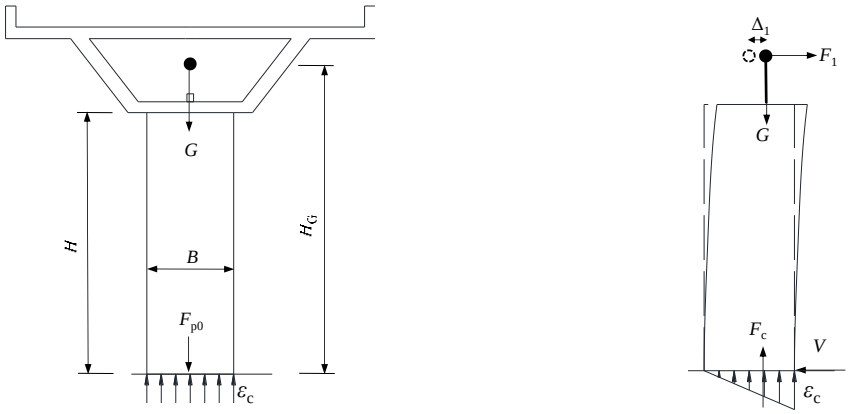

(a) Event 0 (b) Event 1

Fig. 3 Before gap opening

produces a resultant force F_c at bottom surface. In the analytical model, H represents the column height and H_G represents the distance between mass centroid of the superstructure and column bottom surface. Taking the rectangular cross section for example, B and b represents the width and depth of the section, respectively. F_{p0} represents the initial post-tensioning force. The superstructure is simplified as the mass connected to the column through a rigid link.

At event 1, vertical force equilibrium is satisfied as

$$F_c = G + F_{p0} \tag{1}$$

where

$$F_c = \int_0^B b \cdot \sigma(\varepsilon) dx \tag{2.1}$$

$$\varepsilon = \frac{x}{B} \cdot \varepsilon_c \tag{2.2}$$

where $\sigma(\varepsilon)$ denotes the concrete stress dependent on the strain ε. Concrete stress was calculated using the BGL model (Braga *et al*. 2006), which considers the confining effect produced by rectangular stirrups and external wrapping (i.e., FRP material). When ε exceeds the ultimate strain ε_{cu}, concrete crashes and no longer provides any strength. ε_{cu} could be calculated according to Scott *et al*. (1982). The strain of the outermost fiber ε_c is calculated from Eq. (1). According to the moment equilibrium about the centroid of bottom surface, Eq. (3) can be obtained as

$$\int_0^B b \cdot (x - 0.5B) \cdot \sigma(\varepsilon) dx = F_1 \cdot H_G + G \cdot \Delta_1 \tag{3}$$

where

$$\Delta_1 = \frac{F_1 \cdot H^3}{3E_c \cdot I_g} \tag{4}$$

where I_g denotes the cross sectional moment of inertia of column. E_c denotes the concrete elastic modulus which could be calculated according to the *Building Code Requirements for Structural Concrete and Commentary* (ACI 2011)

$$E_c = 33w^{1.5}\sqrt{f_c'} \quad (\text{psi}) \tag{5}$$

where w represents concrete density (lb/ft^3), and f_c' represents the compressive strength of concrete. As a result, F_1 and Δ_1 can be solved by combining Eqs. (3) and (4).

3.2 Rocking

Gap opening commences and propagates at interface following event 1, where θ denotes the rotation angle of column, and c denotes the neutral axis depth, as shown in Fig. 4(a). F_{si} denotes the axial force of the ith bar, with the distance to the rotation toe of y_i. F_p denotes the tendon force, which is not necessarily the same as F_{p0}. Unlike monolithic piers, strain compatibility between concrete and longitudinal reinforcement is violated at member interface after gap opening due to the unbonded PT tendons (and the unbonded length of internal steel bars, if used) (Palermo *et al*. 2007), section equilibrium is thus replaced by global member equilibrium (Pampanin *et al*. 2001, NZS 2006).

The following three equations are obtained according to member equilibrium and compatibility

$$F_c = G + F_p + \sum F_{si} \tag{6}$$

$$F_2 \cdot (H_G + \Delta_{ver}) + G \cdot \Delta_2 = M_c + \sum F_{si} \cdot (y_i - 0.5B) \tag{7}$$

$$\Delta_2 = \frac{F_2 \cdot H^3}{3E_c \cdot I_g} + H_G \cdot \theta \tag{8}$$

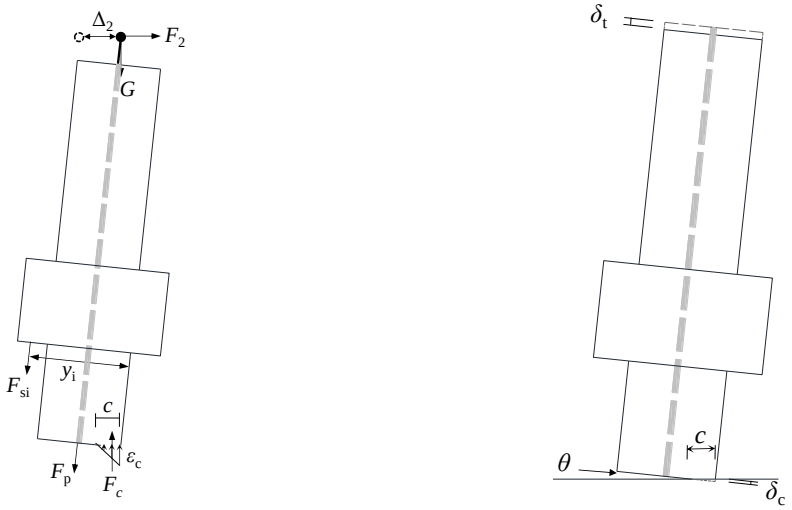

(a) Pier forces (b) Tendon elongation

Fig. 4 Event 2

where M_c represents the moment contribution of F_c to the centroid, and Δ_{ver} represents the possible uplift of mass point due to rocking. For each given Δ_2, three unknown parameters including F_2, θ and c can be solved from the above equations in theory; nevertheless, F_{si} and M_c are expressed by θ and c implicitly, which means the equations cannot be solved directly. Therefore an interective procedure is proposed.

It is evident that F_p=F_{p0} in case $c \leq 0.5B$; otherwise deformation of the tendon concludes two parts: tendon elongation δ_t arising from interface opening, and tendon shortening δ_c arising from concrete column compression, as shown in Fig. 4(b). As a result, increment of the post-tensioning force δF_p is calculated as

$$\delta F_p = k_{pt} \cdot \left[\left(\frac{B}{2} - c \right) \theta - \delta_c \right] \tag{9}$$

where

$$k_{pt} = E_{pt} \cdot A_{pt} / L_{pt} \tag{10.1}$$

$$\delta_c = \delta F_p / k_c \tag{10.2}$$

$$k_c = E_c \cdot A_c / H \tag{10.3}$$

where E_{pt} and A_{pt} are the elastic modulus and total cross section area of the tendon, respectively. L_{pt} is the unbonded length of tendon, and A_c represents the cross section area of the column. To conclude, tendon force is expressed as follows

$$F_p = \begin{cases} F_{p0} & c \geq 0.5B \\ F_{p0} + \dfrac{k_{pt}}{1 + k_{pt}/k_c} \left(\dfrac{B}{2} - c \right) \theta & c < 0.5B \end{cases} \tag{11}$$

On the other hand, axial deformation of the *i*th bar is calculated as

$$d_{\mathrm{i}} = \left(y_{\mathrm{i}} - c\right) \cdot \theta \tag{12}$$

Positive value of d_{i} indicates that the bar is in tension (and negative value for compression). d_{i} consists of two parts, namely d_{ei}, which is the deformation of the elastic part, and d_{pi}, which is the deformation from weakened length. On the other word, d_{i} could be expressed as follows

$$d_{\mathrm{i}} = d_{\mathrm{ei}} + d_{\mathrm{pi}} = \frac{F_{\mathrm{si}}}{k_{\mathrm{ei}}} + L_{\mathrm{pi}} \cdot \varepsilon_{\mathrm{pi}} \tag{13}$$

or written as

$$F_{\mathrm{si}} = k_{\mathrm{ei}} \cdot \left(d_{\mathrm{i}} - L_{\mathrm{pi}} \cdot \varepsilon_{\mathrm{pi}}\right) \tag{14}$$

where k_{ei} denotes the axial stiffness of the elastic segment. L_{pi} and $\varepsilon_{\mathrm{pi}}$ denote the length and strain of weakened part. Eq. (14) cannot be solved directly due to the implicit relationship between F_{si} and $\varepsilon_{\mathrm{pi}}$, detailed procedure for calculating F_{si} is presented in the next section, which is based on a simplified aluminum constructive model.

To solve the resultant force F_{c} at bottom surface, a rational strain distribution assumption along the contact length c is needed. Pampanin *et al*. (2001) pointed out that either triangle or rectangular stress-block could provide acceptable approximation. Another comparison between the plane section hypothesis and the rectangular stress-block assumption showed minor difference on the pier behavior (Guo *et al*. 2012). In the study conducted by Ou *et al*. (2007), linear strain distribution is adopted in the analytical model, showing remarkable difference between 3D finite element simulation regarding the outermost fiber strain; nevertheless the backbone curves of the pier correspond well. Finally, the triangle strain distribution assumed in previous researches is adopted here, as shown in Fig. 4(a), where the resultant force is calculated as

$$F_{\mathrm{c}} = \int_0^c b \cdot \sigma(\varepsilon) dx = \int_0^{\varepsilon_{\mathrm{c}}} b \cdot \frac{c}{\varepsilon_{\mathrm{c}}} \cdot \sigma(\varepsilon) d\varepsilon \tag{15}$$

and M_{c} is expressed as

$$M_{\mathrm{c}} = \int_0^c b \cdot \left(\frac{B}{2} - c + x\right) \cdot \sigma(\varepsilon) dx = F_{\mathrm{c}} \cdot \left(\frac{B}{2} - c\right) + \int_0^{\varepsilon_{\mathrm{c}}} b \cdot \left(\frac{c}{\varepsilon_{\mathrm{c}}}\right)^2 \cdot \varepsilon \cdot \sigma(\varepsilon) d\varepsilon \tag{16}$$

A simplified illustration of outermost fiber strain is shown in Eq. (17), and a more accurate calculation can be found in Ozden and Ertas (2010)

$$\varepsilon_{\mathrm{c}} = \frac{c \cdot \theta}{L_{\mathrm{pl}}} \tag{17}$$

where L_{pl} denotes the plastic hinge length of the equivalent RC column, which is defined as follows (AASHTO 2011)

$$L_{\mathrm{pl}} = 0.08H + 0.15 f_{\mathrm{y}} d_{\mathrm{bl}} > 0.3 f_{\mathrm{y}} d_{\mathrm{bl}} \quad (\mathrm{in}, \mathrm{ksi}) \tag{18}$$

where f_{y} and d_{bl} denotes the yield strength and diameter of longitudinal reinforcement, respectively. To this end, uplift of mass can be expressed as

$$\Delta_{\text{ver}} = \begin{cases} 0 & c \geq 0.5B \\ (0.5B - c)\cdot\theta & c < 0.5B \end{cases} \tag{19}$$

Based on Eqs. (8) to (19), all the variables in Eqs. (6) and (7) can be expressed through θ and c. The proposed iterative procedure consists of one inner loop that solves c for a given θ based on force equilibrium, and one outer loop that solves θ for a given Δ based on member compatibility.

Event 3 is regarded as the ultimate limit state (ULS) and the lateral displacement should not be exceeded. In this paper the following two conditions are considered for this ULS: (1) the PT tendon reaches its maximum tension strain, and (2) column drift reaches a threshold value (i.e., 4.5%). Condition (1) is based on structural global stability and the self-centering capacity provided by the tendon. Condition (2) is set to avoid collapse due to large drift (Dawood and EIGawady 2013). As a result, the displacement of event 3 is

$$\Delta_3 = \min\left[\frac{(\eta\cdot\varepsilon_{\text{u}} - \varepsilon_0)\cdot L_{\text{pt}}\cdot H}{B/2 - c},\quad 0.045H\right] \tag{20}$$

where ε_0 and ε_{u} denotes the initial and ultimate tendon strains, respectively. η is a safety factor whose value could be defined by referring to the maximum tendon force in previous experiment, since minor slip was found after tests (Guo *et al*. 2015); so 0.65 is specified as the value. Besides, the estimation of c has been validated by Sritharan *et al*. (2007). Note that conservative simplification of rigid body deformation (i.e., $\Delta=H\cdot\theta$) is used in condition (1), resulting in a larger calculated tendon strain than the true value.

3.3 Unloading

The gap closes again at event 4, and solution for the curve 2-4 is the same as that of the curve 1-2. The difference between 4 and 1 is the axial force in aluminum bars. At event 5 the lateral force is totally removed, and the condition in Eq. (21) should be satisfied to ensure the self-centering capacity

$$(G + F_{\text{p0}})\cdot\frac{B}{2} \geq \sum F_{\text{si}}\cdot y_{\text{i}} \tag{21}$$

The above equation is a rough estimation on the ratio between restoring force and dissipating force, which can alternatively be simplified as

$$G + F_{\text{p0}} \geq \beta\cdot F_{\text{y}}\sum\left|\frac{2\cdot y_{\text{i}}}{B}\right| \tag{22}$$

where β denotes the overstrength factor and F_{y} denotes the axial force when the bar is yield. A complete solution is shown in the following flow chart. Note that the proposed theory is developed for single pier; for multi-pier bent, the theoretical model could be different depending on the layout of piers, though the basic idea of the pier behavior is similar, i.e., member equilibrium and compatibility.

4. Calculation of dissipator force

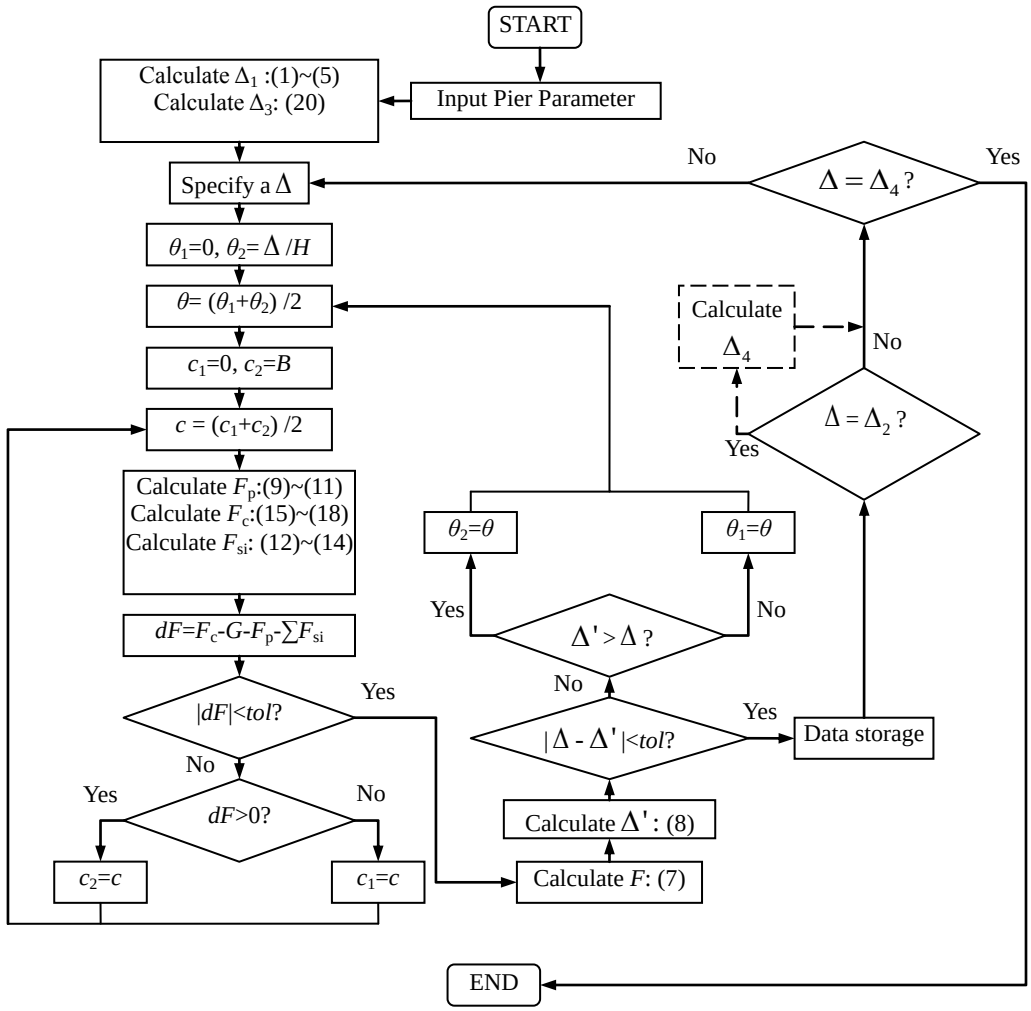

Fig. 5 Analysis flowchart

Dissipator force F_{si} is not given in an explicit manner in Eq. (14) due to the complexity in the working mechanism and constructive model of dissipators. As shown in Fig. 6(a), the total length of the bar is subdivided into three parts: elastic length L_{e1} in the concrete bracket, elastic length L_{e2} below the bracket, and the weakened length L_p. Cross section area of the elastic and weakened segment is A_e and A_p, respectively. As shown in Fig. 6(b), when the bar is in tension, the nut on the bottom surface moves away from the bracket due to bar elongation; when in compression, the bar segment in the bracket (L_{e1}) doesn't work due to the bottom nut, as shown in Fig. 6(c). This working mechanism induces the asymmetry shape of bar force-deformation relationship, as shown in Fig. 6(e). Note that each condition point of the dissipator (i.e., 1 to 5) corresponds to a point in Fig. 6(d).

For the aluminum material, the bilinear kinematic hardening model is adopted. As shown in Fig. 6(d), E_s denotes the elastic modulus and ε_y denotes the yield strain. α denotes the hardening

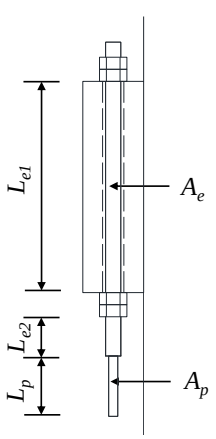

(a) Configuration of bar

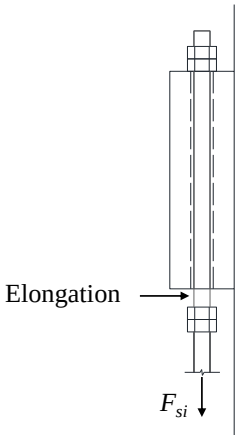

(b) Bar in tension

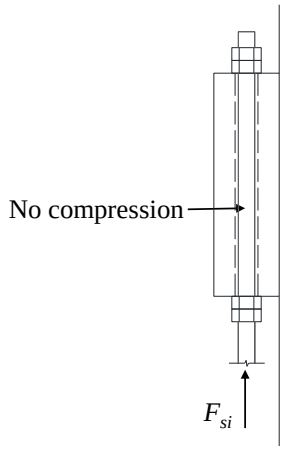

(c) Bar in compression

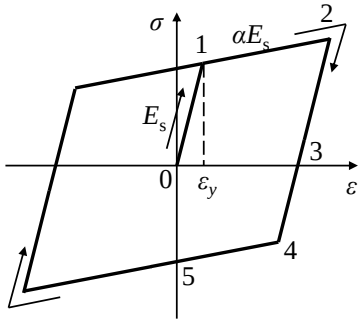

1-yielding (in tension);
2-unloading;
3-total unloading;
4-yielding (in compression);
5-zero strain condition

(d) Constructive model of aluminum

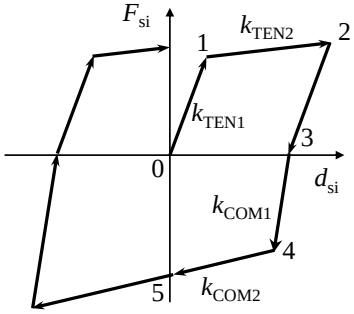

1-yielding of L_p (in tension), and L_{e1} elongates;
2-unloading
3-total unloading of L_p, and L_{e1} returns its original length
4- yielding of L_p (in compression), while L_{e1} does not work
5-dissipator returns its original length

(e) Hysteretic loop of dissipating bar

Fig. 6 Working mechanism of dissipator

ratio. Based on the assumption solution for bar force is transformed into: Given $\theta=\theta_{j-1}$, $c=c_{j-1}$, $F_{si}=F_{j-1}$, $\varepsilon_{pi}=\varepsilon_{j-1}$ in the (j-1)th step, and $\theta=\theta_j$, $c=c_j$ in the jth step, expression for F_{si} in jth step (or F_j) is to be calculated.

Before aluminum yielding, axial stiffness of the weakened segment k_p is expressed as $E_s \cdot A_p/L_p$, and changes to $\alpha \cdot k_p$ after yielding. Aluminum bar in the other segments is assumed to be elastic all the time, and its axial stiffness k_e is expressed as $E_s \cdot A_e/(L_{e1}+L_{e2})$ in tension, while in compression the stiffness k_e' changes into $E_s \cdot A_e/ L_{e2}$. As a result, stiffness of the total bar is expressed in Table 1 and illustrated in Fig. 6(e).

Fig. 7(a) illustrates the loading/unloading behaviour according to the constructive model of aluminum. As shown in Fig. 7(b), for an arbitrary stress-strain condition (ε_{j-1}, σ_{j-1}), yielding strength at two different loading direction can be calculated as

$$\sigma_{\mathrm{y}}=\begin{cases}\sigma_{\mathrm{y1}}=E_{\mathrm{s}}\cdot\varepsilon_{\mathrm{y}}+\dfrac{\alpha}{1-\alpha}\left(E_{\mathrm{s}}\cdot\varepsilon_{\mathrm{j\text{-}1}}-\sigma_{\mathrm{j\text{-}1}}\right)\\ \sigma_{\mathrm{y2}}=-E_{\mathrm{s}}\cdot\varepsilon_{\mathrm{y}}+\dfrac{\alpha}{1-\alpha}\left(E_{\mathrm{s}}\cdot\varepsilon_{\mathrm{j\text{-}1}}-\sigma_{\mathrm{j\text{-}1}}\right)\end{cases} \tag{24}$$

In the iterative procedure, axial deformation of the *i*th bar at the (*j-1*)th step is calculated as

$$d_{\mathrm{j\text{-}1}}=\left(y_{\mathrm{i}}-c_{\mathrm{j\text{-}1}}\right)\cdot\theta_{\mathrm{j\text{-}1}} \tag{25}$$

and axial deformation at the *j*th step is calculated as

$$d_{\mathrm{j}}=\left(y_{\mathrm{i}}-c_{\mathrm{j}}\right)\cdot\theta_{\mathrm{j}} \tag{26.1}$$

$$\delta d_{\mathrm{j}}=d_{\mathrm{j}}-d_{\mathrm{j\text{-}1}} \tag{26.2}$$

Based on the loading behaviour, F_{j} could be calculated from the given $F_{\mathrm{j\text{-}1}}$ and $\delta d_{\mathrm{j\text{-}1}}$, as shown in Table 2.

Table 1 Expression of aluminum bar stiffness

Bar in tension and does not yield	$k_{\mathrm{TEN}}=k_{\mathrm{TEN1}}=\dfrac{1}{1/k_{\mathrm{e}}+1/k_{\mathrm{p}}}$	(23.1)
Bar in tension and yields	$k_{\mathrm{TEN}}=k_{\mathrm{TEN2}}=\dfrac{1}{1/k_{\mathrm{e}}+1/\left(\alpha\cdot k_{\mathrm{p}}\right)}$	(23.2)
Bar in compression and does not yield	$k_{\mathrm{COM}}=k_{\mathrm{COM1}}=\dfrac{1}{1/k_{e}'+1/k_{\mathrm{p}}}$	(23.3)
Bar in compression and yields	$k_{\mathrm{COM}}=k_{\mathrm{COM2}}=\dfrac{1}{1/k_{e}'+1/\left(\alpha\cdot k_{\mathrm{p}}\right)}$	(23.4)

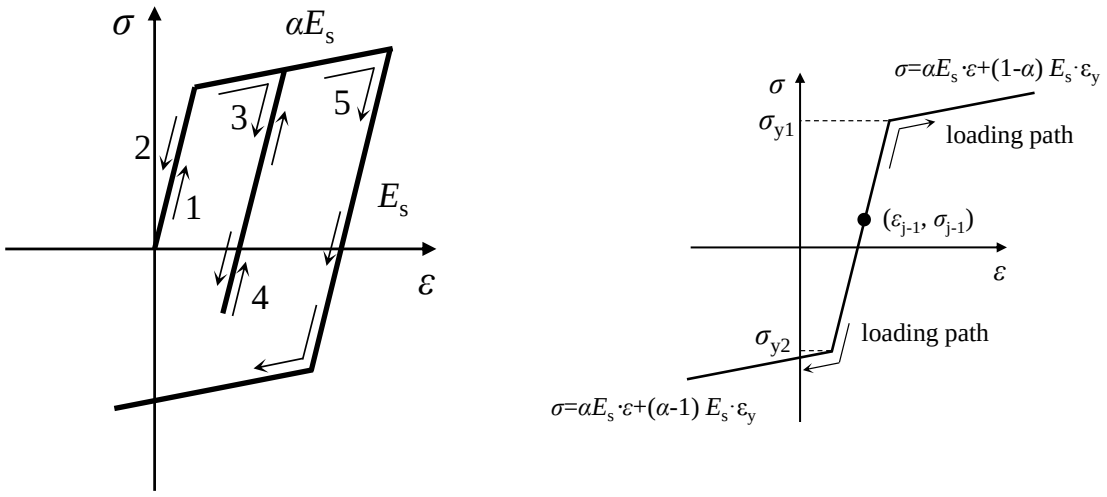

(a) loading and unloading behaviour (b) stress-strain point ($\varepsilon_{\mathrm{j\text{-}1}}$, $\sigma_{\mathrm{j\text{-}1}}$)

Fig. 7 Calculation of σ_{y} corresponding to ($\varepsilon_{\mathrm{j\text{-}1}}$, $\sigma_{\mathrm{j\text{-}1}}$)

Table 2 Expression of aluminum bar force F_j

	$F_j = \begin{cases} F_{j-1} + k_{TEN1} \cdot \delta d_j & d_j < d_{lim} \\ A_p \cdot \sigma_{y1} + k_{TEN2} \cdot (d_j - d_{lim}) & d_j > d_{lim} \end{cases}$	(27)
$F_{j-1}>0, \delta d_j>0$	$d_{lim} = d_{j-1} + \dfrac{A_p \cdot \sigma_{y1} - F_{j-1}}{k_{TEN1}}$	(28)
	$F_j = \begin{cases} F_{j-1} + k_{TEN1} \cdot \delta d_j & d_j > d_{lim1} \\ k_{COM1} \cdot (d_j - d_{lim1}) & d_{lim2} < d_j < d_{lim1} \\ A_p \cdot \sigma_{y2} + k_{COM2} \cdot (d_j - d_{lim2}) & d_j < d_{lim2} \end{cases}$	(29)
$F_{j-1}>0, \delta d_j<0$	$d_{lim1} = d_{j-1} - \dfrac{F_{j-1}}{k_{TEN1}}$	(30.1)
	$d_{lim2} = d_{lim1} + \dfrac{A_p \cdot \sigma_{y2}}{k_{COM1}}$	(30.2)
	$F_j = \begin{cases} F_{j-1} + k_{COM1} \cdot \delta d_j & d_j < d_{lim1} \\ k_{TEN1} \cdot (d_j - d_{lim1}) & d_{lim1} < d_j < d_{lim2} \\ A_p \cdot \sigma_{y1} + k_{TEN2} \cdot (d_j - d_{lim2}) & d_j > d_{lim2} \end{cases}$	(31)
$F_{j-1}<0, \delta d_j>0$	$d_{lim1} = d_{j-1} - \dfrac{F_{j-1}}{k_{COM1}}$	(32.1)
	$d_{lim2} = d_{lim1} + \dfrac{A_p \cdot \sigma_{y1}}{k_{TEN1}}$	(32.2)
	$F_j = \begin{cases} F_{j-1} + k_{COM1} \cdot \delta d_j & d_j > d_{lim} \\ A_p \cdot \sigma_{y2} + k_{COM2} \cdot (d_j - d_{lim}) & d_j < d_{lim} \end{cases}$	(33)
$F_{j-1}<0, \delta d_j<0$	$d_{lim} = d_{j-1} + \dfrac{A_p \cdot \sigma_{y2} - F_{j-1}}{k_{COM1}}$	(34)

Finally, when F_j is obtained, strain along L_p could be expressed through F_j and d_j. If tension strain along L_p exceeds the ultimate strain, the dissipator is regarded as fractured and F_j=0.

5. Stiffness of pier after gap opening

In this section, the influence of θ on pier stiffness along the backbone curve after gap opening is discussed. As shown in Fig. 8, the distance between the resultant force of the bottom surface, F_c, to the extreme fiber at rotation toe is x_c, and two stiffness, namely the secant stiffness and the tangent stiffness are studied. One hypothesis adopted here is that all the dissipators yield after gap opening. This assumption is not appropriate for dissipators near the rotation toe when θ is small; on the other hand, the moment contribution to the toe from these dissipators is also small; therefore, the hypothesis is acceptable. Another hypothesis is that c<0.5B.

5.1 Secant stiffness k_{sec}

According to the moment equilibrium about the point of F_c, the following equation can be

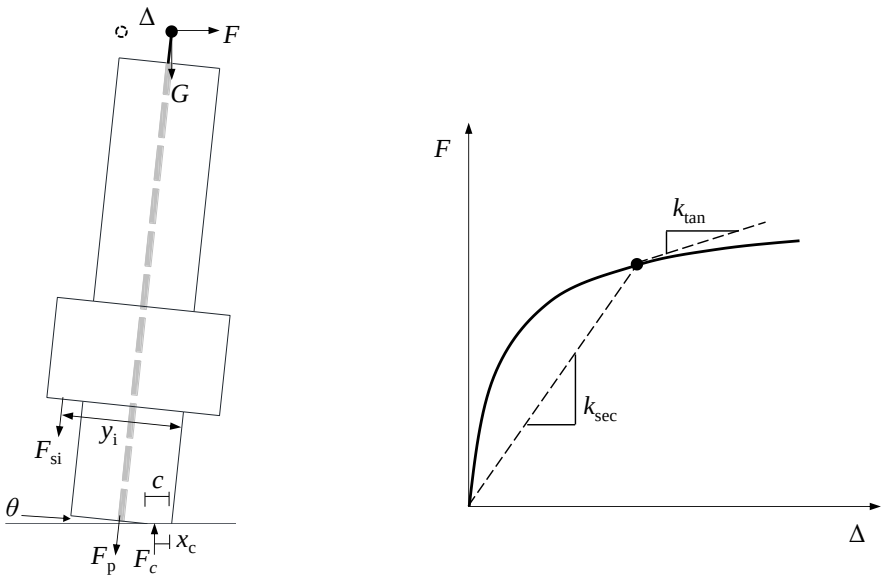

Fig. 8 Stiffness after interface opening

derived

$$F\left[H_{\mathrm{G}}+\left(\frac{B}{2}-c\right)\theta\right]=\left[F_{\mathrm{p0}}+k_{pt}^{'}\left(\frac{B}{2}-c\right)\theta\right]\left(\frac{B}{2}-x_{\mathrm{c}}\right)+G\left(\frac{B}{2}-x_{\mathrm{c}}-\Delta\right)+\sum F_{\mathrm{si}}\cdot\left(y_{\mathrm{i}}-x_{\mathrm{c}}\right) \quad (35)$$

where

$$k_{\mathrm{pt}}^{'}=\frac{k_{\mathrm{pt}}}{1+k_{\mathrm{pt}}/k_{\mathrm{c}}} \quad (36.1)$$

$$F_{\mathrm{si}}=\begin{cases}E_{\mathrm{s}}A_{\mathrm{p}}\varepsilon_{\mathrm{y}}+k_{\mathrm{TEN2}}\left[\left(y_{\mathrm{i}}-c\right)\theta-\dfrac{E_{\mathrm{s}}A_{\mathrm{p}}\varepsilon_{\mathrm{y}}}{k_{\mathrm{TEN1}}}\right] & y_{\mathrm{i}}>0\\ -E_{\mathrm{s}}A_{\mathrm{p}}\varepsilon_{\mathrm{y}}+k_{\mathrm{COM2}}\left[\left(y_{\mathrm{i}}-c\right)\theta-\dfrac{E_{\mathrm{s}}A_{\mathrm{p}}\varepsilon_{\mathrm{y}}}{k_{\mathrm{COM1}}}\right] & y_{\mathrm{i}}<0\end{cases} \quad (36.2)$$

As a result, F_{si} could be simplified as follows

$$F_{\mathrm{si}}=\overline{F_{\mathrm{yi}}}+k_{\mathrm{i}}\left(y_{\mathrm{i}}-c\right)\theta \quad (37)$$

where $\overline{F_{\mathrm{yi}}}$ and k_{i} are only associated with y_{i}. Considering the small rotation angle of the column, there is

$$H_{\mathrm{G}}+\left(\frac{B}{2}-c\right)\theta\approx H_{\mathrm{G}} \quad (38)$$

and Eq. (35) could be transformed into

$$H_{\mathrm{G}}\frac{F}{\theta}=\frac{G+F_{\mathrm{p0}}+\sum\overline{F_{\mathrm{si}}}}{\theta}\cdot\left(\frac{B}{2}-x_{\mathrm{c}}\right)+\left(\overline{M_{\mathrm{pt}}}+\overline{M_{\mathrm{s}}}-G\cdot H\right) \tag{39}$$

where

$$\overline{F_{\mathrm{si}}}=\overline{F_{\mathrm{yi}}}\cdot\frac{y_{\mathrm{i}}-x_{\mathrm{c}}}{\mathrm{B/2}-x_{\mathrm{c}}} \tag{40.1}$$

$$\overline{M_{\mathrm{pt}}}=k_{pt}^{'}\left(\frac{B}{2}-c\right)\left(\frac{B}{2}-x_{\mathrm{c}}\right) \tag{40.2}$$

$$\overline{M_{\mathrm{s}}}=\sum k_{\mathrm{i}}\left(y_{\mathrm{i}}-c\right)\left(y_{\mathrm{i}}-x_{\mathrm{c}}\right) \tag{40.3}$$

Introducing Eq. (8) into Eqs. (39) and (40), the secant stiffness can be expressed as

$$k_{\mathrm{sec}}=\frac{F}{\Delta}=\frac{1}{\dfrac{H^{3}}{3E_{\mathrm{c}}\cdot I_{\mathrm{g}}}+\dfrac{H\cdot H_{\mathrm{G}}}{\dfrac{G+F_{\mathrm{p0}}+\sum\overline{F_{\mathrm{si}}}}{\theta}\cdot\left(\dfrac{B}{2}-x_{\mathrm{c}}\right)+\left(\overline{M_{\mathrm{pt}}}+\overline{M_{\mathrm{s}}}-G\cdot H\right)}} \tag{41}$$

According to Eq. (41), it is concluded that k_{sec} is determined by three variables: θ, c and x_{c}. In practice, the SCPC piers should be designed with relatively small axial compression ratios, so as to mitigate concrete toe crushing during rocking, causing a quick decrease of neutral axis depth c after gap opening. In other words, providing θ is not very small, c and x_{c} could be taken as constant values. As a result, k_{sec} is a function of θ. When θ is close to zero, k_{sec} is similar to the stiffness of monolithic piers; when θ increases k_{sec} drops, causing a changing period of bridge under an earthquake. On the other hand, it is concluded from Eq. (41) that increasing initial PT force or applying dissipator results in an increased k_{sec}.

5.2 Tangent stiffness k_{tan}

If c and x_{c} could be seen as constant values, and when the following approximation is adopted,

$$H_{\mathrm{G}}+\left(\frac{B}{2}-c\right)\theta\approx H_{\mathrm{G}},\quad \Delta\approx H\cdot\theta$$

the total differential form of Eq. (35) can be obtained as

$$H_{\mathrm{G}}dF=k_{pt}^{'}\left(\frac{B}{2}-c\right)\left(\frac{B}{2}-x_{\mathrm{c}}\right)d\theta-GHd\theta+\sum k_{\mathrm{i}}\left(y_{\mathrm{i}}-c\right)\left(y_{\mathrm{i}}-x_{\mathrm{c}}\right)d\theta \tag{42}$$

or

$$H_{\mathrm{G}}\frac{dF}{d\theta}=\overline{M_{\mathrm{pt}}}+\overline{M_{\mathrm{s}}}-GH \tag{43}$$

and the tangent stiffness can be expressed as

$$k_{\tan} = \frac{dF}{d\Delta} = \frac{1}{\dfrac{H^3}{3E_c \cdot I_g} + \dfrac{H \cdot H_G}{\overline{\overline{M_{pt}}} + \overline{M_s} - GH}} \tag{44}$$

From Eq. (44), it is concluded that after gap opening, the tangent stiffness of the pier has a constant value, which is not influenced by the initial post-tensioning force. This conclusion is based on the assumption that the constructive model of aluminum obeys the bilinear kinematic model, and that c and x_c could be taken as constant values. Another conclusion is that a large G or H may produce negative $k_{\tan}$, which corresponds to the possible overturning of bridge.

6. Equivalent viscous damping ratio

Energy dissipation behavior of a structure is evaluated using the equivalent viscous damping ratio. RC pier dissipates energy by forming plastic hinges, and structure damage includes concrete cracking/crushing, and reinforcement yielding/buckling. On the other hand, energy dissipation of the self-centering pier is mainly from the aluminum bars while the main structure remains elastic, so that the post-earthquake repair costs could be minimized.

As shown in Fig. 9, a structure with single degree of freedom is simplified as a mass point with the stiffness of K and damping coefficient of c. $F(t)$ and u represents the imposed force and the resulting displacement, respectively. $F(t)=F_0 \cdot \sin\omega t$, $u(t)=u_0 \cdot \sin(\omega t-\varphi)$, viscous damping force $F_D=cu'$, and F_D could be expressed as

$$F_D = -c\omega u_0 \cos(\omega t - \varphi) = \pm c\omega u_0 \sqrt{1-\sin^2(\omega t-\varphi)} = \pm c\omega u_0 \sqrt{u_0^2 - u^2} \tag{45}$$

$$\left(\frac{F_D}{c\omega u_0}\right)^2 + \left(\frac{u}{u_0}\right)^2 = 1 \tag{46}$$

As shown in Fig. 9, the area W_D within the ellipse is the energy dissipated by F_D in one cycle, which is expressed as

$$W_D = \int cu'\,du = \int_0^{2\pi/\omega} cu'^2 dt = \int_0^{2\pi/\omega} c[\omega u_0 \cos(\omega t - \varphi)]^2 dt = \pi c\omega u_0^2 = 2\pi\xi \frac{\omega}{\omega_n} k u_0^2 \tag{47}$$

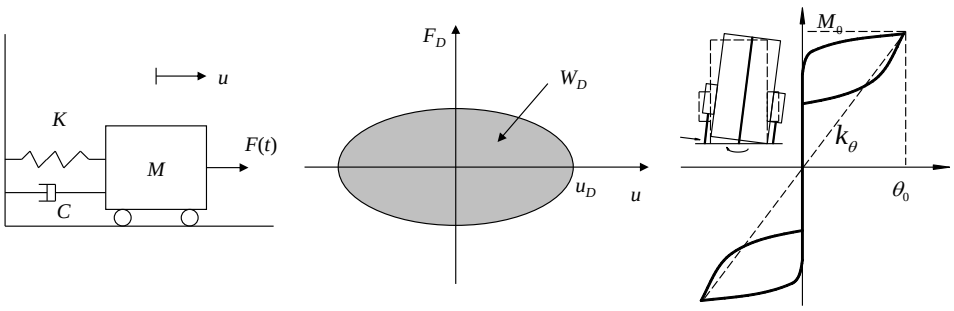

Fig. 9 Oscillator viscous damping and self-centering pier energy dissipation

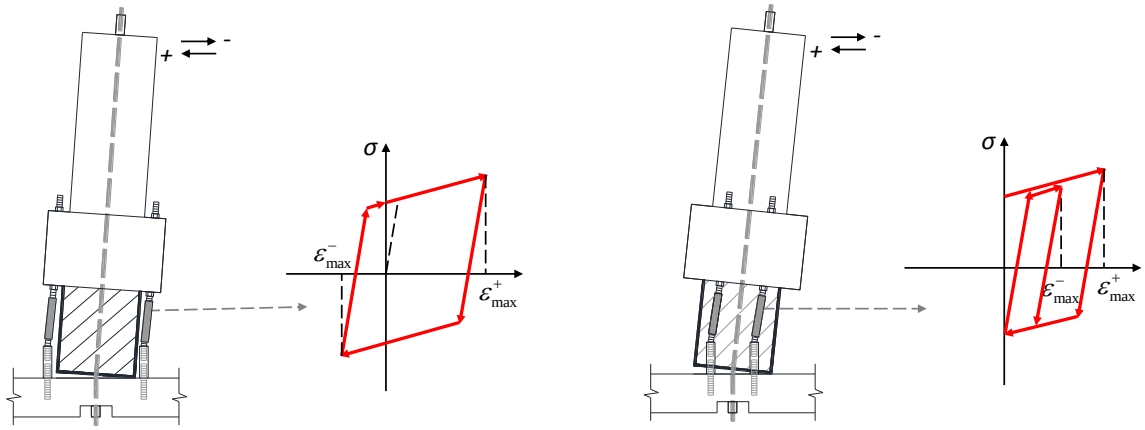

Fig. 10 Strain history of the weakened segment

where ω and ω_n denotes the circular frequency of $F(t)$ and structure, respectively. k and ζ denote the structural lateral stiffness and viscous damping ratio, respectively. As shown in Fig. 9, accurate calculation of the area within the flag-shaped hysteretic loop of the self-centering pier is complex in that strain history of weakened segment is associated with c, and constructive model of aluminum is not ideally bilinear. A rough estimation for the equivalent viscous damping ratio is given in this paper, based on the assumption that c=0.

Fig.10 demonstrates the stress-strain of the dissipator at two different positions. As a result, energy dissipation of the ith dissipator in one cycle is

$$W_i = 2E_s \cdot A_p \cdot \varepsilon_y \cdot L_p \left(\varepsilon^+_{max} + \left|\varepsilon^-_{max}\right| - 4\varepsilon_y\right) \tag{48}$$

where

$$\varepsilon^+_{max}, \varepsilon^-_{max} \geq 2\varepsilon_y \tag{49}$$

According to the definition of viscous damping, $W_D = \sum W_i$, k=k_0, and the equivalent viscous damping ratio can be obtained by taking ω/ω_n=1, and k_0=F_0/u_0 (shown in Fig. 9)

$$\xi_{eq} = \frac{E_s \cdot A_p \cdot \varepsilon_y \cdot L_p}{\pi F_0 u_0} \cdot \sum \left(\varepsilon^+_{max} + \left|\varepsilon^-_{max}\right| - 4\varepsilon_y\right) \tag{50}$$

7. Validation through existing test results

Previously, one 1:3 scaled self-centering pier with external dissipators was constructed and tested at the Key Laboratory of Concrete and Prestressed Concrete of Ministry of Education at Southeast University, as shown in Fig. 11 (Guo *et al*. 2015). Tensile test results of aluminum bar showed that the stress-strain curve could be matched by a bilinear model where E_s, ε_y, α is 70 GPa, 2.36×10^{-3} and 0.01, respectively. Another tensile test showed that the prestressed tendons which were made of basalt FRP (BFRP) remained basically elastic before a sudden burst out of the fibers

and loss of strength. Elastic modulus and ultimate stress of the tendon was measured 44 GPa and 1080 MPa, respectively. Longitudinal reinforcement consisted of 16 Φ 10 rebars that were distributed evenly along the circumference, producing a reinforcement ratio of 1.03%. Concrete cubic strength was measured as 41.8 MPa.

In total, five tests were conducted and the detailed information is listed in Table 3. Test results are demonstrated in Fig. 12, where Tests 1 and 2 showed bilinear hysteresis since that no dissipators were attached to the column; a higher initial prestress force can postpone gap opening, but it does not affect the secant stiffness after gap opening, as validated in Section 5.2. Test 3 exhibits a higher load-carrying capacity and superior dissipation capacity than Test 4, and this is because moment contribution from bars at east/west sides to the rotation toe is larger than that from bars at south/north sides. In Test 3, four aluminum bars broke successively during the last cycle while the calculated strains are smaller than the ultimate strain. The unexpected failure calls for a further study of bar ductility under cyclic loading. Besides, the analytical model fails to predict bar fracture, since the ultimate strain was obtained from tensile test; in other words, ductility of aluminum was impaired under cyclic loading. This issue is improved in Test 5 by increasing the length of weakened part, and the stable energy dissipation is observed. After the tests, no visible damage was observed in the column, and maximum residual drift among the tests was no larger than 0.3%, which shows the superiority of the proposed the self-centering pier.

Validations of pier hysteresis are shown in Fig. 12. It is found that the proposed analytical procedure could well catch the backbone curves, though the predicted residual drifts are slightly lower than the tested ones, which may be caused by simplified material model and slip at column-foundation interface. Note that Tests 3 and 4 exhibit a "slip" type of behavior in the unloading branches. One possible reason is that the screws of aluminum bars (with relatively low strength) experienced minor damage during the reversal loading, making the contact between nuts and concrete corbel loose. Note that the nuts are made of high strength steel. However, when the unloading continued, the nuts and the concrete corbel gradually became tightly contact again, and the structural stiffness was recovered. Besides, validations of the tangent and secant stiffness of the backbone curve are shown in Fig. 13, where lateral drifts at 0.25%, 2%, 4% are selected for comparison. In general, the difference in secant stiffness is relatively small, though the deviation between the test and analytical results regarding tangent stiffness is comparatively large, especially for Test 3.

Validation of the equivalent viscous damping ratio is shown in Fig. 14, while ξ is calculated using Eq. (47) and Eq. (50), respectively. For test 1 and test 2, there is no dissipator in the pier and ξ is zero by the proposed model. On the other hand, the test results exhibit an equivalent viscous damping ratio about 2%~5% for these two tests, which may arises from inner friction of the actuator, minor damage of concrete toes. For test 3 in the last cycle, the tested ξ is much larger than the analytical result, which can be explained as follows: Four dissipating bars broke successively during the last cycle, causing a moderate decrease of W_D, but a sharp decrease of k (see Eq. (47)); in this way ξ is increased. For the analytical model, this phenomenon did not occur, which calls for further improvement of the model. For test 4 and 5, the analytical results match well with the tests ones.

Validation on PT force is shown in Fig. 15. Since the PT tendons were placed in the middle of the pier cross-section, the force-drift relationship is symmetric. Note that the relationship is not absolutely V-shaped as the force changed mildly with drift close to zero, which is due to the elastic deformation of pier under small loading. Minor prestress loss was observed after the test, which was different from analytical result, and this was probably due to tendon slip, plastic deformation

in the anchorage and/or at the pier toes (Guo *et al.* 2015). On the other hand, self-centering capacity of the pier is impaired due to prestress loss.

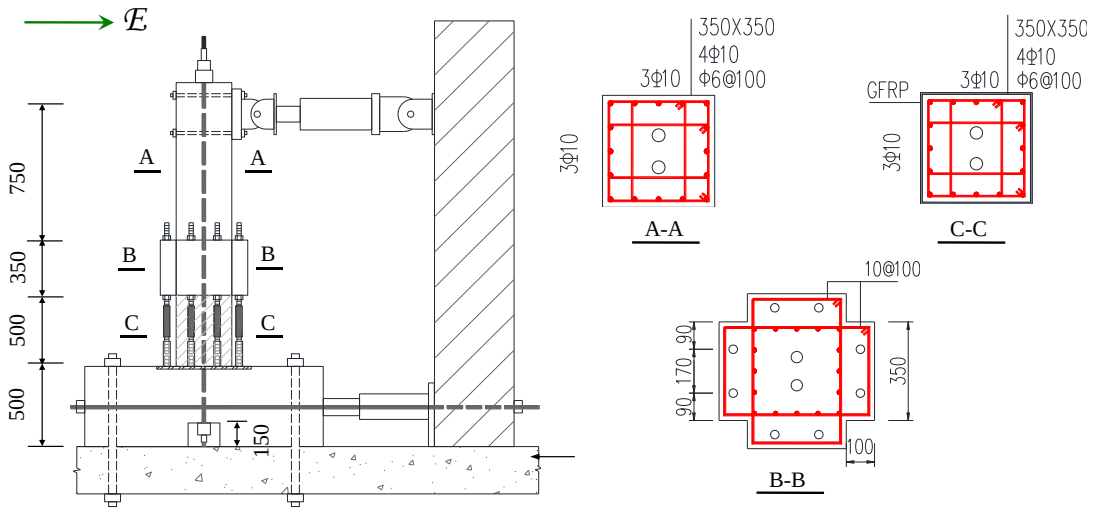

Fig. 11 Specimen configuration (mm)

Table 3 Test parameters

Test	F_{p0} (kN)	Number of bars	Bar position	A_e (mm^2)	A_p (mm^2)	L_p (mm)	A_{e2} (mm)	L_p(mm)*
1	120	0						193
2	220	0						193
3	220	4	East &West	490.9	176.7	100	150	193
4	220	4	South & North	490.9	176.7	100	150	193
5	220	4	East & West	490.9	176.7	200	50	193

Note*: L_p is calculated based on Eq. (18)

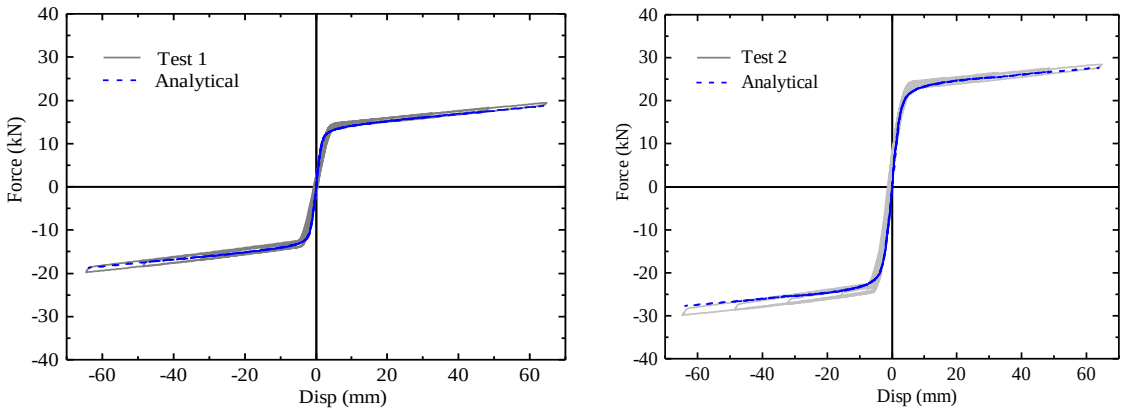

Fig. 12 Comparison of hysteresis

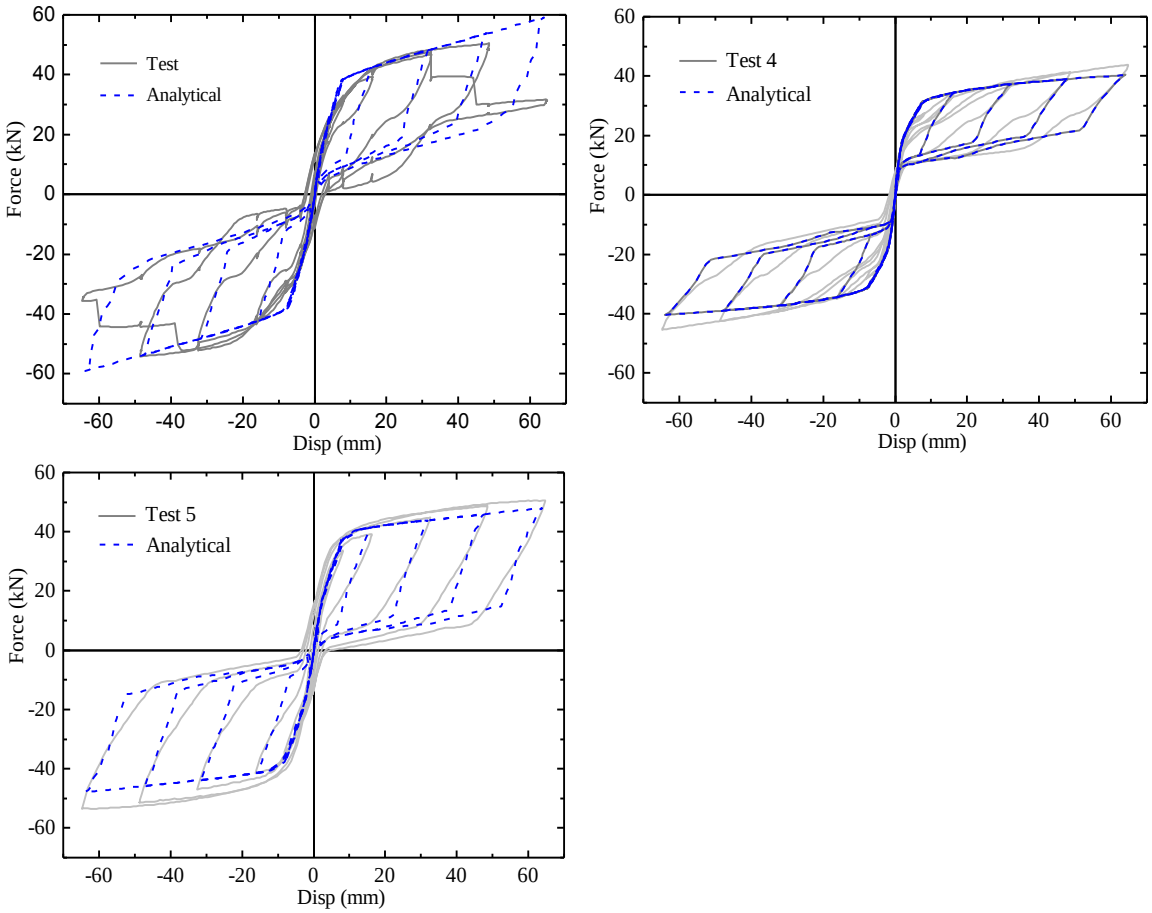

Fig. 12 Continued

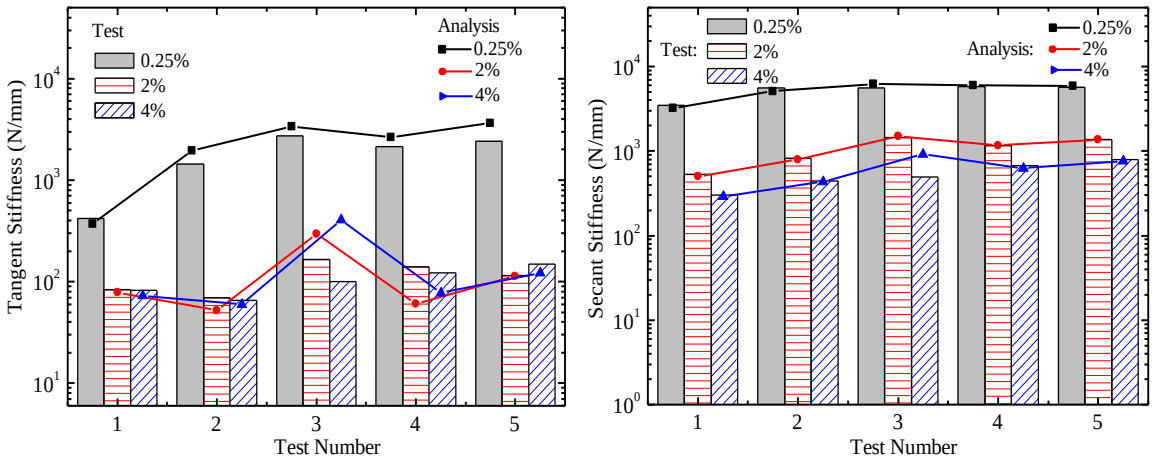

(a) Validation of tangent stiffness (b) Validation of secant stiffness

Fig. 13 Comparison of pier stiffness

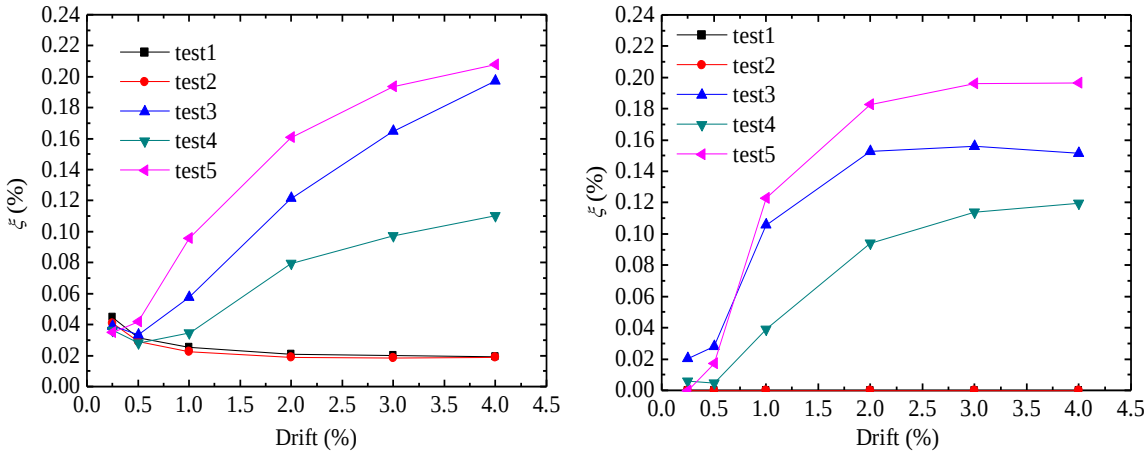

(a) Test results (b) Analytical results

Fig. 14 Comparison of equivalent viscous damping ratio

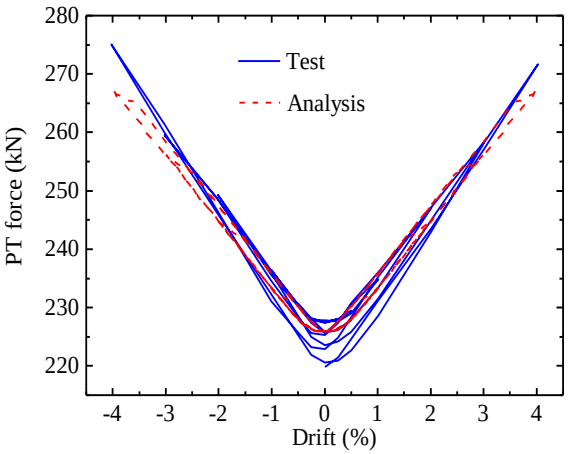

Fig. 15 Comparison of PT force

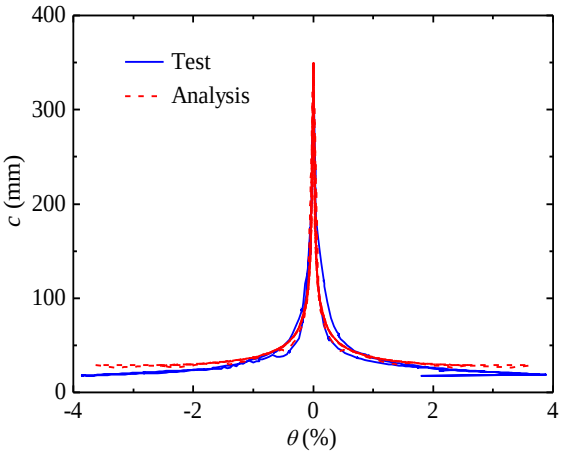

Fig. 16 Comparison of c (Test 3)

Validation on the neutral axis depth, c, is shown in Fig. 16. The curve was roughly symmetric, with a sharp reduction in c when θ increased from zero to 0.5%; however, this reduction became mild after θ exceeded 1%, with c dropping from around 35 mm to 20 mm. However, the maximum measured θ was slightly smaller than 4%, indicating that lateral displacement may have some contribution from pier bending.

8. Conclusions

In this paper, a novel self-centering pier with external dissipators is proposed and the hysteretic behavior is theoretically investigated. Conclusions of the presented study are as follows:

(1) The hysteretic behavior of the pier is characterized by a flag shape under cyclic loading. The pier behaves like a monolithic one before gap opening, and after that the pier rocks and the

lateral stiffness is provided by prestressed tendons and the dissipators. Structural damage is mainly in the external ED bars while the other members remain elastic. After earthquake residual deformation is negligible and the bridge could be brought into operation after replacing the damaged aluminum bars.

(2) A trial and error process incorporating member equilibrium and compatibility is introduced in this paper to calculate the force-displacement relationships under cyclic loading. Considering the complexity in bar working mechanism, a bilinear kinematic hardening constructive model is proposed and the dissipator deformation is calculated based on four different situations. Based on the proposed model, it is concluded that a larger secant stiffness k_{sec} is obtained by increasing initial prestress force F_{p0} or using more dissipators, while tangent stiffness k_{tan} is not affected by F_{p0}. On the other hand, larger gravity of superstructure and slenderness of the pier tend to produce a negative k_{tan}, indicating the possible overturning of the bridge that should be avoided.

(3) To validate the analytical model, cyclic test results of a 1:3 scaled specimen are used. The proposed model could catch the backbone curves and secant stiffness well, while significant difference exists between the analytical and test tangent stiffness, which may arise from the error prediction of occurrence of rocking, simplification of aluminum constructive model, and the premature failure of the dissipators.

(4) Equivalent viscous damping ratio is estimated based on the bilinear kinematic hardening model of aluminum and a simplification of strain history of dissipators. Inner friction of the actuator and dissipating bar fracture were not taken into consideration, resulting in a difference between the results. However, this difference became much smaller when the drift ratio exceeds 1%.

(5) The relationship between PT force and lateral drift ratio is not absolute V-shaped as the force changed mildly with drift close to zero, which was due to the elastic deformation of pier under small loading. Minor prestress loss which was probably due to tendon slip, plastic deformation in the anchorage and/or at the pier toes, was observed after the test.

(6) The rupture of dissipaters, which is related to the low cycle fatigue of bars under reversed loads, is not fully captured by the theoretical model, due to that indicating that a more rational constructive model of aluminum may be needed in future study so that the strength degradation during the reversal loading could be considered.

Acknowledgments

The research described in this paper was financially supported by the Natural Science Foundation of China under grants No. 51378107 and 51078075, the Education Department of Jiangsu under Grant No. JHB2012-1, the Fok Ying Tung Education Foundation under Grant No. 131074, and the Open Foundation of National Engineering Laboratory for High Speed Railway Construction under Grant No.HSR2013029.

References

AASHTO (2011), *Guide Specifications for LRFD Seismic Bridge Design*, Washington: American Association of State Highway and Transportation Officials.

ACI 318-11 (2011), *Building Code Requirements for Structural Concrete (ACI 318-11) and Commentary*

(ACI 318R-11), American Concrete Institute, USA.
Braga, F., Gigliotti, R. and Laterza, M. (2006), "Analytical stress-strain relationship for concrete confined by steel stirrups and/or FRP jackets ", *J. Struct. Eng*., **132**(9), 1402-1416.
Chou, C.C. and Chen, Y. (2006), "Cyclic tests of PT precast CFT segmental bridge columns with unbonded strands", *J. Earthq. Eng. Struct. Dyn.*, **35**(2), 159-175.
Chou, C.C. and Hsu, C.P. (2008), "Hysteretic model development and seismic response of unbonded PT precast CFT segmental bridge columns", *J. Earthq. Eng. Struct. Dyn*., **37**(6), 919-934
Dawood, H.M. and ElGawady, M. (2013), "Performance-based seismic design of unbonded precast PT concrete filled GFRP tube piers", *Compos. Part B: Eng*., **44**(1), 357-367.
ElGawady, M., Booker, A.J. and Dawood, H.M. (2010), "Seismic behavior of posttensioned concrete-filled fiber tubes", *J. Compos. Constr*., **14**(5), 616-628.
Guo, Jia, Xin Ke, Gui and He Ming, Hua (2012), "Experimental study and analysis on the seismic performance of a self-centering bridge pier", *J. Eng. Mech*., **29**(Sup 1), 29-34. (in Chinese)
Guo, T., Cao, Z.L., Xu, Z.K. and Lu, S. (2015), "Cyclic load tests on self-centering concrete pier with external dissipators and enhanced durability", *J. Struct. Eng.*, doi: 10.1061/(ASCE)ST.1943-541X.0001357.
Hewes, J.T. and Priestley, M.J.N. (2002), "Seismic design and performance of precast concrete segmental bridge columns", Rep. No. SSRP-2001/25, University of California at San Diego, USA.
Kawashima, K., MacRae, G.A., Hoshikuma, J.I. and Nagaya, K. (1998), "Residual displacement response spectrum", *J. Struct. Eng*., **124**(5), 523-530.
Kurama, Y.C., Weldon, B.D. and Shen, Q. (2006), "Experimental evaluation of posttensioned hybrid coupled wall subassemblages", *J. Struct. Eng*., **132**(7), 1017-1029.
Mander, J.B. and Cheng, C.T. (1997), "Seismic resistance of bridge piers based on damage avoidance design", Technical Report NCEER-97-0014 (National Centre for Earth. Eng. Research), State University of New York, Buffalo.
Marriott, D., Pampanin, S. and Palermo, A. (2009), "Quasi static and pseudo dynamic testing of unbonded post tensioned rocking bridge piers with external replaceable dissipators", *J. Earthq. Eng. Struct. Dyn*., **38**(3), 331-354.
New Zealand Standards (NZS) (2006), "Appendix B: Special provisions for the seismic design of ductile jointed precast concrete structural systems", NZS 3101:2006, Concrete standard, Wellington, New Zealand.
Stanton, J., Stone, W.C. and Cheok, G.S. (1997), "A hybrid reinforced precast frame for seismic regions", *J. PCI*, **42**(2), 20-32.
Palermo, A., Pampanin, S. and Calvi, G.M. (2005), "Concept and development of hybrid solutions for seismic resistant bridge systems", *J. Earthq. Eng*., **9**(6), 899-921.
Palermo, A., Pampanin, S. and Marriott, D. (2007), "Design, modeling, and experimental response of seismic resistant bridge piers with posttensioned dissipating connections", *J. Struct. Eng*., **133**(11), 648-1661.
Palermo, A., Pampanin, S. and Buchanan, A.H. (2006), "Experimental investigations on LVL seismic resistant wall and frame subassemblies", *First European Conference on Earthquake Engineering and Seismology*, Geneva, Switzerland.
Pampanin, Priestley and Sritharan (2001), "Analytical modeling of the seismic behavior of precast concrete frames designed with ductile connections", *J. Earthq. Eng*., **5**(3), 329-367.
Priestley, M.J.N. and Tao, J.R. (1993), "Seismic response of precast prestressed concrete frames with partially debonded tendons", *PCI J*., **38**(1), 58-67.
Ou, Y.C. (2007), "Precast segmental PT concrete bridge columns for seismic regions", Ph.D. Dissertation, State University of New York.
Ou, Y.C., Chiewanichakorn, M., Aref, A.J. and Lee, G.C. (2007), "Seismic performance of segmental precast unbonded posttensioned concrete bridge columns", *J. Struct. Eng*., **133**(11), 1636-1647.
Ou, Y.C., Wang, P.H., Tsai, M.S., Chang, K.C. and Lee, G.C. (2009), "Large-scale experimental study of precast segmental unbonded posttensioned concrete bridge columns for seismic regions", *J. Struct. Eng*.,

136(3), 255-264.
Ozden, S. and Ertas, O. (2010), "Modeling of pre-cast concrete hybrid connections by considering the residual deformations", *Int. J. Physic. Sci*., **5**(6), 781-792.
Pampanin, S., Nigel Priestley, M.J. and Sritharan, S. (2001), "Analytical modeling of the seismic behavior of precast concrete frames designed with ductile connections", *J. Earthq. Eng*., **5**(3), 329-367.
Scott, B.D., Park, R. and Priestley, M.J.N. (1982), "Stress-strain behavior of concrete confined by overlapping hoops at low and high strain rates", *ACI J*., **79**(1), 13-27.
Sritharan, S., Aaleti, S. and Thomas, D.J. (2007), "Seismic analysis and design of precast concrete jointed wall systems", ISU-ERI-Ames report, Ames (Iowa): Department of Civil, Construction and Environmental Engineering, Iowa State University.
Takeda, T., Sozen, M.A. and Nielsen, N.N. (1970), "Reinforced concrete response to simulated earthquakes", *J. Struct. Div*., **96**(12), 2557-2573.

KT

Nomenclature

A_c	Cross section area of column	k_e'	axial stiffness of elastic segment of bar in compression
A_e	cross section area of bar elastic segment	k_p	axial stiffness of weakened segment of bar
A_p	cross section area of bar weakened segment	k_{TEN}	axial stiffness of bar in tension
A_{pt}	total cross section area of prestressed tendon	k_{tan}	tangent stiffness of pier
B	column section width	k_{sec}	secant stiffness of pier
b	column section depth	L_{e1}	length of bar elastic segment in the bracket
c	neutral axis depth at column bottom	L_{e2}	length of bar elastic segment below the bracket
d_{bl}	diameter of longitudinal reinforcement	L_{pi}	length of weakened segment of ith bar
d_{ei}	axial deformation of elastic segment of ith bar	L_{pl}	plastic hinge length of equivalent RC column
d_i	axial deformation of ith bar	L_{pt}	unbonded length of prestressed tendon
d_{pi}	axial deformation of weakened segment of ith bar	M_c	moment contribution of F_c to the centroid of cross section
E_c	elastic modulus of concrete	w	concrete density
E_c	elastic modulus of concrete	y_i	distance between ith bar and rotation toe
E_{pt}	elastic modulus of prestressed tendon	α	hardening ratio of aluminum
E_s	elastic modulus of aluminum	β	over strength factor of bar
F	lateral force of superstructure	Δ	lateral displacement of superstructure
F_c	vertical resultant force at pier bottom surface	ε_0	initial strain of tendon
F_p	prestressed tendon force	ε_c	concrete strain at outermost fiber
F_{p0}	initial post-tensioning force	ε_{cu}	ultimate strain of concrete material
F_{si}	axial force of the ith dissipating bar	ε_{pi}	strain of weakened segment of ith bar
F_y	yield force of dissipating bar	ε_u	ultimate strain of tendon
f_c'	compressive strength of concrete	ε_y	yield strain of aluminnum
f_y	yield strength of longitudinal reinforcement	η	safety factor

G weight of superstructure
H pier column height
I_g moment of inertia of column section
k_{COM} axial stiffness of bar in compression
k_e axial stiffness of elastic segment of bar in tension
θ rotation angle of column
ξ_{eq} Equivalent viscous damping ratio
$\sigma(\varepsilon)$ material stress dependent on strain ε
σ_y aluminum yield strength corresponding to current strain
$(\cdot)_j$ Variation $(\cdot)$ at jth step